Robotica (2017) volume 35, pp. 2036–2055. © Cambridge University Press 2016
doi:10.1017/S0263574716000709

A comparative study of two model-based control techniques for the industrial manipulator

Ahmet Dumlu†*, Köksal Erentürk†, Alirıza Kaleli‡ and Kağan Koray Ayten†

†*Department of Electrical and Electronics Engineering, College of Engineering, Ataturk University, 25240 Erzurum, Turkey. E-mails: keren@atauni.edu.tr, kagan.koray@erzurum.edu.tr*
‡*Department of Mechatronics Engineering, College of Engineering, Ataturk University, 25240 Erzurum, Turkey. E-mail: arizakaleli@atauni.edu.tr*

(Accepted September 10, 2016. First published online: October 17, 2016)

SUMMARY
In this paper, design, analysis and real-time trajectory tracking control of a 6-degree of freedom revolute spherical-spherical type parallel manipulator, actuated by six hybrid stepper motors, has been studied. Two different control approaches have been used to improve the trajectory tracking performance of the designed manipulator. The first approach considered a single input-single output (SISO) linear quadratic regulator (LQR) for trajectory tracking control of the manipulator. Another controller type based on a nonlinear sliding mode controller method has been utilized to take decoupled dynamic approximation model of the manipulator into account and to improve tracking performance of the manipulator. Real-time experimental results for the two different control techniques have been verified. Finally, according to the results, the nonlinear sliding mode controller method has improved the tracking performance of the designed manipulator.

KEYWORDS: Parallel manipulator, kinematics analysis, dynamics analysis, hybrid stepper motor, linear quadratic optimal regulator control, sliding mode control.

1. Introduction

Parallel manipulators with a closed-loop kinematic chain, generally exhibit advantages such as high stiffness, speed, accuracy and large loading capacity when compared with serial manipulators.[1,2] Due to these advantages, parallel manipulators have been used in wide areas, including flight simulators,[3] medical operations,[4–7] machine tools,[8–10] micro-motion[11] and pick-and-place operations in industry.[12,13]

Main mechanical characteristic of parallel manipulators is closed-loop kinematic structure, which includes a moving platform that is connected to a fixed base via multiple limbs or legs and every limb is controlled using one actuator individually. In general, parallel manipulators have more complicated kinematics and dynamic analysis compared with conventional serial manipulators due to the closed-loop kinematic structure and actuators working against each other.

It is possible to change the architecture of the manipulator according to the type of joints and actuators used in the structure of parallel manipulators. In the area of 6-degrees-of-freedom (6-DOF) parallel mechanisms, most of the researchers have particularly focused on the most popular architecture, namely the 6-SPS (spherical, prismatic and spherical) Stewart parallel manipulator. This type of manipulator has been generally actuated by hydraulic actuators.[14,15] Another type of 6-DOF parallel mechanism architecture, known as 6-RSS (revolute, spherical, and spherical) parallel manipulator, is introduced by Castaneda and Takeda.[16] This type of parallel manipulators can also be used for abovementioned applications.[17–19] When 6-RSS parallel manipulator is compared to the 6-SPS ones, 6-RSS parallel manipulator is less studied by the researchers due to its complicated non-linear dynamics model.

*Corresponding author. E-mail: ahmetdumlu@erzurum.edu.tr

https://doi.org/10.1017/S0263574716000709 Published online by Cambridge University Press

A 6-RSS parallel manipulator is actuated by electrical motors, which are connected to input links with revolute joints. Therefore, this architecture is called a motor-mechanism coupling system in the literature.[20−22] Due to the presence of the coupling characteristics, the dynamic model of the system includes highly time-varying nonlinearities. In addition, the uncertainty of the motor-mechanism coupling system parameters, such as un-modelled system dynamics and undesirable disturbance effects, makes control of the system difficult.[15] When the overall system is considered, it is very crucial to design a controller with great efficiency to execute the system smoothly. In practice, manipulators are controlled to track a desired trajectory that is planned in their workspace. In recent years, various advanced control techniques have been performed and successfully implemented to control 6-DOF SPS Stewart parallel manipulators accurately, such as proportional integral derivative PID control,[23,24] linear quadratic regulator (LQR) control,[25] model-based control,[26−29] H∞ adaptive control,[30−31] computed torque control,[32] fuzzy control[33] and sliding mode control (SMC).[34−37]

Among these control techniques, SMC is a variable structure and also an efficient robust control method for nonlinear systems with unknown loads and un-modelled dynamics. A sliding mode controller has been successfully implemented in many nonlinear systems for improving their performance and robustness against disturbances and perturbations, reducing model order, simplifying design and improving tracking performance as explained by[38,39]. Other characteristic features of SMC are that a systematic approach provided by the sliding mode controller improves the ability of the system to overcome the stability maintaining problem and also increases the performance of the system for modelling imprecisions.[40] Because of the characteristic feature of the SMC listed above, many researchers used this technique to overcome control problem in their systems.

In this paper, unlike the most focused traditional 6-DOF SPS parallel manipulators in the scientific literature, an SMC is performed for the first time on a designed and modelled 6-DOF-RSS parallel manipulator for high-accuracy trajectory tracking control of the manipulator. Additionally, in order to show the advantages of the SMC over other classical control techniques, the LQR control method has been applied to the manipulator as a second control approach. In order to compare the two control techniques, the velocity and position analyses of the manipulator have been realized initially by using the geometrical method. In addition to this, two approaches have been considered to create the dynamics model of the manipulator. The first approach is a linearized model based on a single link approximation of the manipulator for implementation of linear quadratic regulator controller design. The second approach is a decoupled dynamic model approximation of the manipulator for the implementation of the sliding mode controller, which adapts itself to uncertainties in the model and to nonlinearities generally associated with a parallel manipulation. The primary contribution of this paper is the design, implementation and evaluation of an LQR and of SMC techniques for the motion control of the 6-DOF RSS parallel manipulators. In order to execute the real-time performance of the both controllers, experimental studies have been realized. It has been validated experimentally that SMC is an efficient, robust control method for the manipulator including un-modelled dynamics.

This paper is organized as follows. The designed system structure has been presented in Section 2. Section 3 describes kinematic and dynamic analyses of the manipulator. Both linear quadratic optimal regulator and nonlinear SMC strategies have been introduced in Section 4. The experimental results have been presented in Section 5, followed by the concluding remarks in Section 6.

2. System Description

Figure 1 shows the designed 6-DOF RSS type parallel manipulator. The manipulator consists of a fixed platform, a moving platform and six identical limbs connecting the moving platform to the fixed platform. Each limb consists of an input link and a coupler link (passive link) that are connected together with a spherical joint. Moreover, each input link has been coupled to the shaft of the hybrid stepper motor with a revolute joint and each coupler link has been coupled to the moving platform with a spherical joint. Using this structure, it is possible for the moving platform to move with 6 spatial DOF, effectively.[18]

3. Analysis and Mathematical Modelling of the Manipulator

A schematic diagram of the manipulator, offset angle distributions of the fixed and moving platforms and vector representation of a single chain of the manipulator are depicted in Figs. 2–4.

https://doi.org/10.1017/S0263574716000709 Published online by Cambridge University Press

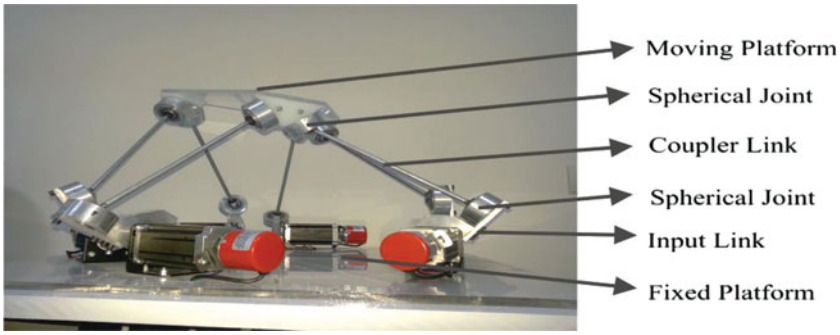

Fig. 1. 6-DOF RSS type manipulator.

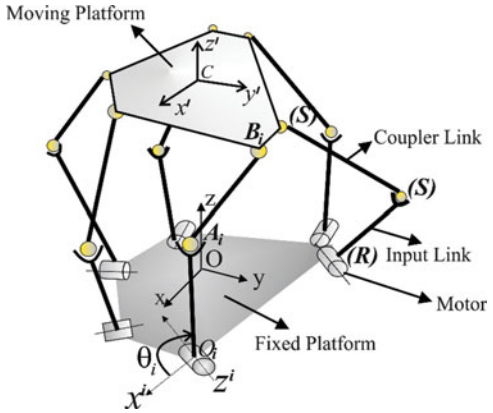

Fig. 2. Schematic diagram of the manipulator.

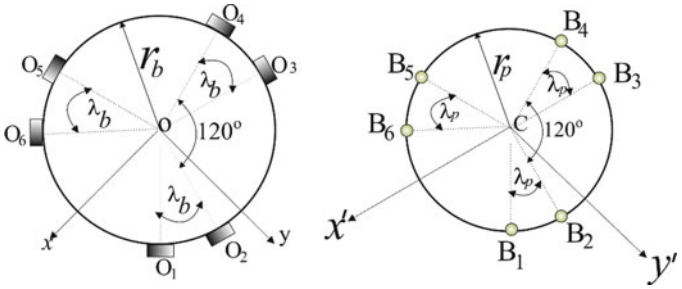

Fig. 3. Offset angle distributions of the fixed platform (right) and the moving platform (left).

For the purpose of analysis, a fixed coordinate frame x, y, z is attached to the fixed platform and a mobile coordinate frame x', y', z' is attached to the moving platform. As shown in Figs. 2 and 3, the points O_i and B_i (in this paper $i = 1 \cdots 6$) have been symmetrically arranged on the circumference, fixed and moving platforms with radii r_b and r_p, and offset angles λ_b and λ_p, respectively.

As shown in Fig. 4, the centre of the first spherical joints is denoted by A_i and the centre of the second spherical joints is attached to the mobile platform by B_i. Each point A_i moves along a circular trajectory referred to as track i whose centre has been denoted by O_i. In order to simplify the analysis, the following assumption has been made: Each actuated revolute joint can rotate fully, without any restriction. Corresponding parameters of the manipulator and the design parameters have been listed in Table I.

3.1. Inverse kinematic problem of manipulator

In this study, a geometrical approach has been used for the kinematic analysis of the manipulator. Geometrically, for each leg, the problem can be regarded as finding of the intersection point(s) between a sphere of radius l_2 at centre B_i and the circle track. Clearly, depending on the position of

https://doi.org/10.1017/S0263574716000709 Published online by Cambridge University Press

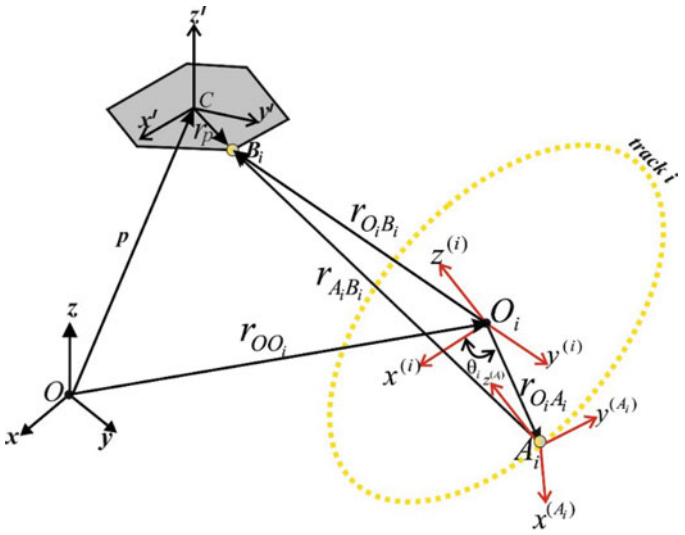

Fig. 4. Vector representation of a single chain of the RSS parallel mechanism.

Table I. Parameters of manipulator.

Notations	Descriptions
$\boldsymbol{p}$	Position vector of the moving platform with respect to the fixed coordinate frame.
R	Orientation matrix, which can be represented by Euler transformation with respect to the fixed coordinate frame. The orientation matrix can be expressed in terms of the direction cosines of x', y', z' as follows: $R = \begin{bmatrix} c\phi c\theta c\psi - s\phi s\psi & -c\phi c\theta s\psi - s\phi c\psi & c\phi s\theta \\ s\phi c\theta c\psi + c\phi s\psi & -s\phi c\theta s\psi + c\phi c\psi & s\phi s\theta \\ -s\phi c\psi & s\theta s\psi & c\theta \end{bmatrix}$
θ_i	Actuator angle (ith input variable) is measured from $x^{(i)}$ axis to O_iA_i
$[x^{(i)},\ y^{(i)}, z^{(i)}]$	Track frame axes with centre at point O_i.
R_i	Orientation of track frame i with respect to the fixed coordinate frame. This matrix is given as follows: $R_i = \begin{bmatrix} \cos(\theta_i) & 0 & \sin(\theta_i) \\ \sin(\theta_i) & 0 & -\cos(\theta_i) \\ 0 & 1 & 1 \end{bmatrix}$
$[x^{(A_i)},\ y^{(A_i)},\ z^{(A_i)}]$	Coupler link frame axes with centre at point A_i. The $z^{(A_i)}$ axis is always parallel to the track frame's $z^{(i)}$ axis, and the $x^{(A_i)}$ axis is always along line O_iA_i, pointing away from O^i.
l_1	Length of input links (magnitude of vector $\boldsymbol{r}_{O_iA_i}$) (Design parameter → 82 mm)
l_2	Length of coupler links (magnitude of vector $\boldsymbol{r}_{A_iB_i}$) (Design parameter → 285 mm)
r_b	Radius of fixed platform (magnitude of vector $\boldsymbol{r}_{OO_i}$) (Design parameter → 250 mm)
r_p	Radius of moving platform (magnitude of vector $\boldsymbol{r}_{CB_i}$) (Design parameter → 145 mm)
λ_b	Offset angles of the fixed base platform (Design parameters → [0, 100, 120, 220, 240, 340] deg)
λ_p	Offset angles of the moving platform (Design parameters → [32,5 67,5 152,5 187,5 272,5 307,5] deg)
m_{l_1}	Mass of the input link (Design parameter → 0.184 kg)
m_{l_2}	Mass of the coupler link (Design parameter → 0.085 kg)
m_p	Mass of the moving platform (Design parameter → 0.483 kg)

https://doi.org/10.1017/S0263574716000709 Published online by Cambridge University Press

point B_i, this problem may have an infinite number of real solutions, two solutions, a single one, or none at all.

According to geometrical relationships, the vector of $\boldsymbol{r}^{(i)}_{A_iB_i}$ relative to the $(x^{(i)},\ y^{(i)}, z^{(i)})$ coordinate frame can be written as

$$\boldsymbol{r}^{(i)}_{A_iB_i} = \boldsymbol{r}^{(i)}_{O_iB_i} - \boldsymbol{r}^{(i)}_{O_iA_i}. \tag{1}$$

By squaring both sides of Eq. (1), one can obtain the main equation constituting the inverse kinematic problem given by Eq. (2):

$$l_2^2 = \varrho_i^2 + l_1^2 - 2\left(\boldsymbol{r}^{(i)}_{O_iB_i}\right)^T \boldsymbol{r}^{(i)}_{O_iA_i} \tag{2}$$

where $\varrho_i = r^{(i)}_{O_iB_i}$, $\boldsymbol{r}^{(i)}_{O_iB_i} = R_i^T(\boldsymbol{p} + R\boldsymbol{r'}_{\boldsymbol{p}} - \boldsymbol{r}_{OO_i})$.

Using $\boldsymbol{r}^{(i)}_{O_iA_i} = l_1[\ \cos\theta_i \quad \sin\theta_i \quad 0\ ]^T$ and components of $\boldsymbol{r}^{(i)}_{O_iB_i}$ $(x^{(i)}_{B_i}, y^{(i)}_{B_i}$ and $z^{(i)}_{B_i})$, Eq. (2) can be written as a function of input variable θ_i as follows:

$$x^{(i)}_{B_i}\cos\theta_i + y^{(i)}_{B_i}\sin\theta_i = \frac{\varrho_i^2 + l_1^2 - l_2^2}{2l_1} \equiv p_i. \tag{3}$$

In order to have a real solution to this equation, the following inequality should hold true:

$$x^{(i)^2}_{B_i} + y^{(i)^2}_{B_i} - p_i^2 \equiv \Gamma_i \geq 0. \tag{4}$$

Unless $p_i^2 = x^{(i)^2}_{B_i} + y^{(i)^2}_{B_i}$, there exist two real solutions for Eq. (3), determined uniquely from

$$\sin\theta_i = \frac{p_i y^{(i)}_{B_i} + x^{(i)}_{B_i}\delta_i\sqrt{\Gamma_i}}{x^{(i)^2}_{B_i} + y^{(i)^2}_{B_i}}, \qquad \cos\theta_i = \frac{p_i x^{(i)}_{B_i} - y^{(i)}_{B_i}\delta_i\sqrt{\Gamma_i}}{x^{(i)^2}_{B_i} + y^{(i)^2}_{B_i}} \tag{5}$$

where $\theta_i \in [-\pi, \pi]$ and $\delta_i = \pm 1$ is the branch index. Hence, input variable θ_i is found using Eq. (6):

$$\theta_i = a\tan2\left(\sin\theta_i, \cos\theta_i\right). \tag{6}$$

3.2. Velocity Jacobian of the manipulator

Referring to Fig. 4, a closed-loop equation for the ith limb of the RSS parallel manipulator can be written as follows:

$$\boldsymbol{p} + \boldsymbol{r}_{CB_i} = \boldsymbol{r}_{OO_i} + \boldsymbol{r}_{O_iA_i} + \boldsymbol{r}_{A_iB_i}. \tag{7}$$

Differentiating Eq. (7) with respect to time yields

$$\boldsymbol{V}_p + \boldsymbol{\omega}_p \times \boldsymbol{r}_{CB_i} = \boldsymbol{\omega}_{O_iA_i} \times \boldsymbol{r}_{O_iA_i} + \boldsymbol{\omega}_{A_iB_i} \times \boldsymbol{r}_{A_iB_i} \tag{8}$$

where $\boldsymbol{V}_p$ and $\boldsymbol{\omega}_p$ are the linear and angular velocities of the moving platform, respectively; $\boldsymbol{\omega}_{O_iA_i}$ and $\boldsymbol{\omega}_{A_iB_i}$ are the angular velocities of the ith limb.

For this manipulator, the input vector is $\overrightarrow{\dot{q}} = [\dot\theta_1,\ \dot\theta_2, \dot\theta_3,\ \dot\theta_4,\ \dot\theta_5, \dot\theta_6]^T$, and the output vector is $\overrightarrow{X} = [V_{x'}, V_{y'}, V_{z'}, \dot\Phi,\ \dot\theta,\ \dot\psi]^T$. All other joint rates are passive variables. To eliminate the passive joint rate, multiplying the both sides of Eq. (8) by $\boldsymbol{r}_{A_iB_i}$ in dot product form results in the following equation:

$$\boldsymbol{r}_{A_iB_i} \cdot \boldsymbol{V}_p + \boldsymbol{\omega}_p \cdot \left(\boldsymbol{r}_{CB_i} \times \boldsymbol{r}_{A_iB_i}\right) = \boldsymbol{\omega}_{O_iA_i} \cdot \left(\boldsymbol{r}_{O_iA_i} \times \boldsymbol{r}_{A_iB_i}\right). \tag{9}$$

https://doi.org/10.1017/S0263574716000709 Published online by Cambridge University Press

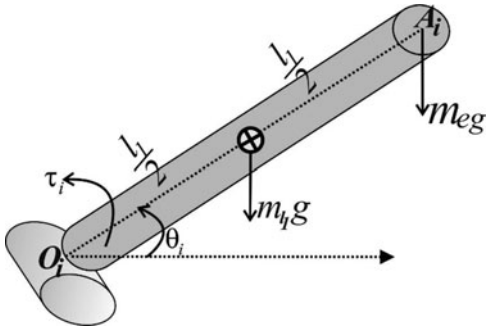

Fig. 5. Single link model of manipulator.

After some algebraic operation, Eq. (9) has been arranged in the matrix form and J_x and J_q has been obtained in the following form:

$$J_x \dot{X} = J_q \dot{q}. \tag{10}$$

Hence, the overall Jacobian matrix, defined as the coefficient matrix of any set of equations that relate the velocity state of the moving platform to the actuated joint rates, can be rewritten as

$$\dot{q} = J\dot{X}, \quad \left(J = J_q^{-1} J_x\right). \tag{11}$$

3.3. Dynamics of the manipulator

In order to investigate the effects of the manipulator dynamics and control techniques, two modelling approaches have been developed without consideration of the friction of the passive joints. The first approach is based on a single link approximation of the manipulator for the single input-single output (SISO) modelling. This SISO model has been used for linear quadratic optimal control implementation. Secondly, decoupled dynamic model approximation has been developed to obtain the manipulator dynamical model. This modelling approach is preferable for nonlinear control techniques such as a sliding mode controller to keep the nonlinear systems under control.

3.3.1. Single link dynamic model approximation. A schematic diagram of the single link model has been shown in Fig. 5, where g is the acceleration due to gravity, m_{l_1} is the mass of the input link, θ_i is the angular displacement of the input link from the base of the manipulator and τ_i is the applied torque by the actuator for the ith input link. It assumes that the mass of the moving platform, m_p, has been evenly divided between the six legs and concentrated at the end of the input link. Similarly, the mass of each coupler link, m_{l_2}, has been concentrated at the end of the input link. Equivalent mass m_{eq} has been expressed in Eq. (12) for this approximation.

$$m_{eq} = m_{l_2} + \frac{m_p}{6}. \tag{12}$$

This model also assumes that each link can be modelled separately so that it neglects the influence of the motion of the rest of the manipulator on the input link modelled. Both of these assumptions are substantial, but these assumptions are made to obtain provide a dynamic model that will allow the development of linear quadratic optimal control of the manipulator. The equation of the motion for the simplified link model for the ith leg is found by summing the torques about the revolute joint and by applying Euler's equation of motion, which is given by

$$\tau_i = \left(\frac{1}{3} m_{l_1} l_1^2 + m_{\text{eq}} l_1^2 + I_m\right) \ddot{\theta}_i + c_d \dot{\theta}_i + l_1 g \left(\frac{1}{2} m_{l_1} + m_{\text{eq}}\right) \cos\left(\theta_i\right). \tag{13}$$

3.3.2. Decoupled dynamic model approximation. The Newton Euler approach has been used to obtain decoupled dynamic model of the manipulator. The dynamic model of the manipulator includes high

https://doi.org/10.1017/S0263574716000709 Published online by Cambridge University Press

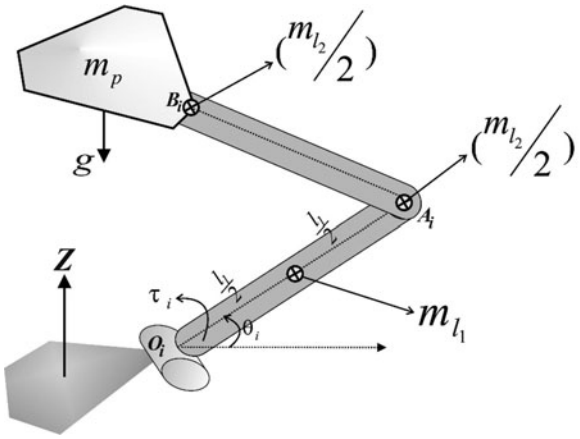

Fig. 6. Schematic of the ith leg of the manipulator.

nonlinearity and calculation burden process. As shown in Fig. 6, this dynamic model has assumed that the mass of each coupler link (m_{l_2}) has been divided and concentrated between the joints A_i and B_i. This assumption can be made because the coupler links' mass of the designed manipulator is lighter than the rest of the manipulator mass and the coupler links do not play an effective role in the manipulator dynamics.

After making the assumptions above, the equation of the motion is written by summing the moments about the actuated joint (O_i) for the ith leg:

$$\sum M_{O_i} = I_J \ddot{\theta}_i + c_d \dot{\theta}_i + \tau^*_{mp,i}. \tag{14}$$

Mathematical expressions of I_J and $\tau^*_{mp,i}$ have been given by Eq. (15):

$$I_J = \frac{1}{3} m_{l_1} l_1^2 + \frac{1}{2} m_{l_2} l_1^2 + I_m \tag{15}$$

$$\tau^*_{mp,i} = (J^T)^{-1} K \ddot{X}$$

$$K = \begin{bmatrix} m & 0 & 0 & 0 & 0 & 0 \\ 0 & m & 0 & 0 & 0 & 0 \\ 0 & 0 & m & 0 & 0 & 0 \\ 0 & 0 & 0 & \frac{mr_p}{4} & 0 & 0 \\ 0 & 0 & 0 & 0 & \frac{mr_p}{2} & 0 \\ 0 & 0 & 0 & 0 & 0 & \frac{mr_p}{2} \end{bmatrix}$$

where J is the Jacobian matrix, $\ddot{X}$ is the acceleration of the moving platform and m is equal to $m = 3m_{l_2} + m_p$.

Due to the actuator torques and the gravitational force, an expression for the resultant moment at point O_i for all of the six legs is given by

$$\begin{bmatrix} \sum M_{J_{1,0}} \\ \sum M_{J_{2,0}} \\ \cdot \\ \cdot \\ \cdot \\ \sum M_{J_{6,0}} \end{bmatrix} = \begin{bmatrix} \tau_1 \\ \tau_2 \\ \cdot \\ \cdot \\ \cdot \\ \tau_6 \end{bmatrix} - \frac{1}{2} l_1 m_{l_1} g \begin{bmatrix} \cos(\theta_{1,0}) \\ \cos(\theta_{2,0}) \\ \cdot \\ \cdot \\ \cdot \\ \cos(\theta_{6,0}) \end{bmatrix} - \frac{1}{4} l_1 m_{l_2} g \begin{bmatrix} \cos(\theta_{1,0}) \\ \cos(\theta_{2,0}) \\ \cdot \\ \cdot \\ \cdot \\ \cos(\theta_{6,0}) \end{bmatrix} - (J^T)^{-1} K \begin{bmatrix} 0 \\ 0 \\ g \\ 0 \\ 0 \\ 0 \end{bmatrix}. \tag{16}$$

https://doi.org/10.1017/S0263574716000709 Published online by Cambridge University Press

Substituting Eqs. (15) and (16) into Eq. (14) as written for six legs and solution of the actuator torques can be obtained in the following form:

$$\begin{bmatrix} \tau_1 \\ \tau_2 \\ . \\ . \\ . \\ \tau_6 \end{bmatrix} = \frac{1}{2} l_1 g \left(m_{l_1} + \frac{1}{2} m_{l_2} \right) \begin{bmatrix} \cos\left(\theta_{1,0}\right) \\ \cos\left(\theta_{2,0}\right) \\ . \\ . \\ . \\ \cos\left(\theta_{6,0}\right) \end{bmatrix} + \left(J^T\right)^{-1} K \begin{bmatrix} 0 \\ 0 \\ g \\ 0 \\ 0 \\ 0 \end{bmatrix} + I_J \begin{bmatrix} \ddot{\theta}_{1,0} \\ \ddot{\theta}_{2,0} \\ . \\ . \\ . \\ \ddot{\theta}_{6,0} \end{bmatrix} + \left(J^T\right)^{-1} K \ddot{X} + c_d \begin{bmatrix} \dot{\theta}_{1,0} \\ \dot{\theta}_{2,0} \\ . \\ . \\ . \\ \dot{\theta}_{6,0} \end{bmatrix}. \tag{17}$$

Using the differential of the Jacobian given by Eq. (11), one can obtain the acceleration of the moving platform ($\ddot{X}$) in terms of the manipulator joint angles. These relations have been given by Eq. (18):

$$\ddot{X} = J^{-1} \begin{bmatrix} \ddot{\theta}_1 \\ \ddot{\theta}_2 \\ . \\ . \\ . \\ \ddot{\theta}_6 \end{bmatrix} + \frac{d}{dt} \left(J^{-1}\right) \begin{bmatrix} \dot{\theta}_1 \\ \dot{\theta}_2 \\ . \\ . \\ . \\ \dot{\theta}_6 \end{bmatrix}. \tag{18}$$

Substituting Eq. (18) into Eq. (17), the general dynamic model of the manipulator has been given by Eq (19):

$$\tau = M(q)\,\ddot{q} + C(q, \dot{q})\,\dot{q} + G(q), \tag{19}$$

where the state $q = [\theta_1, \theta_2 \ldots \theta_6]^T$ is a vector with six actuator angles, $M(q)$ is the mass matrix, $C(q, \dot{q})$ is the Coriolis and centrifugal force, $G(q)$ is the gravitational force and τ is the actuator torques and mathematical expressions for these terms have been given by Eq (20):

$$\begin{aligned} M(q) &= I_J \mathrm{I} + \left(J^T\right)^{-1} K J^{-1} \\ C(q, \dot{q}) &= c_d \mathrm{I} + \left(J^T\right)^{-1} K \frac{d}{dt} \left(J^{-1}\right) \\ G(q) &= \frac{1}{2} l_1 g \left(m_{l_1} + \frac{1}{2} m_{l_2} \right) \begin{bmatrix} \cos(\theta_1) & \ldots & \cos(\theta_6) \end{bmatrix}^T \left(J^T\right)^{-1} K \begin{bmatrix} 0 & 0 & g & 0 & 0 & 0 \end{bmatrix}^T \\ \tau &= \begin{bmatrix} \tau_1 & \ldots & \tau_6 \end{bmatrix}^T. \end{aligned} \tag{20}$$

3.4. Actuator dynamics

The designed parallel manipulator is actuated by the hybrid stepper motor. The hybrid stepping motor is an AC two-phase synchronous motor with two phases A and B in quadrature for low-speed applications. However, unlike the conventional AC motors, the hybrid stepping motor does not have a clear equivalent circuit for time domain equation analysis. However, using the permanence-based method, one can obtain the equivalent magnetic circuit of the hybrid stepping motor, from which the basic voltage equations can be deduced. Thus, the motor can be represented by the following electric equations:[41]

$$\begin{aligned} u_a &= R i_a + L \frac{d}{dt} i_a - K_m \omega \sin(N\theta) \\ u_b &= R i_b + L \tfrac{d}{dt} i_b - K_m \omega \cos(N\theta) \end{aligned} \tag{21}$$

where i_a and i_b are the currents of the phases A and B, u_a and u_b are the phase voltages, R is the phase resistance (1.5 Ω), L is the phase inductance (6.5 mH), K_m is the torque constant (0.000455 Nm · s/rad) and N is the step number of the rotor and is equal to 50. ω is the angular

https://doi.org/10.1017/S0263574716000709 Published online by Cambridge University Press

velocity and θ is the mechanical rotor position. It is clear that θ and ω coincide with the angular position and velocity of the input link ($[\ q \quad \dot{q}\ ]^T$).

The output torque of the motor, which is determined by the control current, can be expressed as follows:

$$\begin{aligned} \tau_{motor} &= K_m \{-i_a \sin(N\theta) + i_b \cos(N\theta)\} - J_m \frac{d\omega}{dt} - K_v \omega \\ \omega &= \frac{d\theta}{dt} \end{aligned} \tag{22}$$

where K_v is the coefficient of viscous friction ($0.178\,\mathrm{V}\cdot\mathrm{s/rad}$), J_m is the rotary inertia of the rotor ($17.65 \times 10^{-5}\,\mathrm{kg}\cdot\mathrm{m}^2$). Applying the Park transformation to (21) and (22), the model of the HSM in the rotating frame ($d-q$) becomes

$$\begin{aligned} U_d &= Ri_d + L\frac{d}{dt}i_d - Lp\omega i_q \\ U_q &= Ri_d + L\frac{d}{dt}i_q - Lp\omega i_d + K_m\omega \\ \tau_{motor} &= K_m i_q - J_m\frac{d\omega}{dt} - K_v\omega. \end{aligned} \tag{23}$$

According to the output torque of the motor and the manipulator, the motor-mechanism model is formulated from Eqs. (23) and (19) as follows:

$$M(q)\,\ddot{q} + C(q,\dot{q})\,\dot{q} + G(q) = K_m i_q - J_m\ddot{q} - K_v\dot{q}. \tag{24}$$

Rewriting the above equation yields

$$(M(q) + J_m)\ddot{q} + (C(q,\dot{q}) + K_v)\,\dot{q} + G(q) = K_m i_q. \tag{25}$$

For simplicity, Eq. (25) could be rewritten as

$$M(q)\ \ddot{q} + N(q,\dot{q}) = K_m i_q = \tau(t) \tag{26}$$

where the $N(q,\dot{q})$ vector is $N(q,\dot{q}) = (C(q,\dot{q}) + K_v)\dot{q} + G(q)$.

4. Controller Design

In this study, two different control techniques have been used for trajectory tracking control of the parallel manipulator. The first one is the SISO-based linear quadratic optimal control implementation using the single link model. The second one is SMC for the decoupled dynamic model approximation of the manipulator.

4.1. Linear quadratic optimal control implementation

In this section, the linear optimal control algorithm has been developed with the single link approximation of the manipulator model. For this purpose, this model has been linearized about an operating point. An operating point of the nonlinear system Eq. (13) is $\boldsymbol{x}^* = [\boldsymbol{q}^* \quad \dot{\boldsymbol{q}}^*]^T$ when $u = \tau^*$. The linearization of Eq. (13) has been given by

$$\begin{aligned} \dot{\boldsymbol{\Delta x}} &= A\boldsymbol{\Delta x} + B\Delta u = f\left(\dot{\boldsymbol{\Delta x}}, \boldsymbol{\Delta u}\right) \\ \Delta y &= C\boldsymbol{\Delta x} + D\Delta u = h\left(\boldsymbol{\Delta x}, \Delta u\right) \end{aligned} \tag{27}$$

https://doi.org/10.1017/S0263574716000709 Published online by Cambridge University Press

where

$$\boldsymbol{\Delta x} = \boldsymbol{x} - \boldsymbol{x}^*,\ \Delta u = u - u^*.$$

$$A = \left[\frac{df}{dx}\right]_{x^*,u^*} = \begin{bmatrix} \frac{\partial f_1}{\partial x_1}\left(\boldsymbol{x}^*, u^*\right) & \frac{\partial f_1}{\partial x_2}\left(\boldsymbol{x}^*, u^*\right) \\ \frac{\partial f_1}{\partial x_1}\left(\boldsymbol{x}^*, u^*\right) & \frac{\partial f_1}{\partial x_2}\left(\boldsymbol{x}^*, u^*\right) \end{bmatrix}, \quad B = \left[\frac{df}{du}\right]_{x^*,u^*} = \begin{bmatrix} \frac{\partial f_1}{\partial u}\left(\boldsymbol{x}^*, u^*\right) \\ \\ \frac{\partial f_1}{\partial u}\left(\boldsymbol{x}^*, u^*\right) \end{bmatrix}$$

$$C = \left[\frac{dh}{dx}\right]_{x^*,u^*} = \begin{bmatrix} \frac{\partial h}{\partial x_1}\left(\boldsymbol{x}^*, u^*\right) & \frac{\partial h}{\partial x_2}\left(\boldsymbol{x}^*, u^*\right) \end{bmatrix}, \quad D = \left[\frac{dh}{du}\right]_{x^*,u^*}$$

The optimal control theory is concerned with operating a dynamical system at minimum cost. Linear quadratic regulator is one of the optimal control strategies and this regulation method provides a systematic way of computing the state feedback control gain matrix.

The optimal regulation problem is to determine the gain matrix $\boldsymbol{K}$ optimal control vector $\boldsymbol{u_k} = -\boldsymbol{K}\boldsymbol{x_k}$, so as to minimize the cost function given by Eq. (28):

$$J_{Cost} = \frac{1}{2}\sum_{k=1}^{M}\left[\boldsymbol{x}_k^T\,\boldsymbol{Q}\boldsymbol{x}_k + \boldsymbol{u}_k^T\,\boldsymbol{R}\boldsymbol{u}_k\right] \tag{28}$$

where $\boldsymbol{Q}$ and $\boldsymbol{R}$ are the positive definite real symmetric weighting matrices that are chosen by the designer. These matrices are design parameters and they define the relationship between regulation performance and control efforts.

In order to minimize cost function, Eq. (28) gives the state feedback control law in the following form:

$$\boldsymbol{u_k}(\boldsymbol{t}) = -\boldsymbol{R}^{-1}\boldsymbol{B}^T\boldsymbol{P}\boldsymbol{x_k}(\boldsymbol{t}) \tag{29}$$

where $\boldsymbol{P}$ is the positive-definite matrix. The solution of the Riccati equation given by

$$\boldsymbol{A}\boldsymbol{P} + \boldsymbol{P}\boldsymbol{A} - \boldsymbol{P}\boldsymbol{B}\boldsymbol{R}^{-1}\boldsymbol{B}\boldsymbol{P} + \boldsymbol{Q} = 0. \tag{30}$$

4.2. Sliding mode control design

In the SMC system, joint space trajectories are forced to reach a sliding manifold in finite time that is called the reachability phase and these trajectories are forced to stay on the manifold for all future time in the sliding phase.[42]

The tracking control problem in joint space is to drive the joint position $\boldsymbol{q}$ to the desired position $\boldsymbol{q_d}$. Tracking error $\tilde{q}$;

$$\tilde{\boldsymbol{q}} = \boldsymbol{q} - \boldsymbol{q}_{\boldsymbol{des}}. \tag{31}$$

The sliding surface is determined by the following equation:

$$\boldsymbol{s} = \dot{\tilde{\boldsymbol{q}}} - \boldsymbol{\lambda}\tilde{\boldsymbol{q}} \tag{32}$$

where $\boldsymbol{\lambda} = diag[\lambda_1,\ \lambda_2, \ldots, \lambda_6]$ is a weighting parameter.

The controller design can be translated in terms of finding a control law for the input vector $\boldsymbol{\tau}$ that verifies individual sliding conditions of the form

$$\frac{1}{2}\frac{d}{dt}{s_i}^2 \le -\eta_i\,|s_i| \qquad (\eta_i > 0). \tag{33}$$

Satisfying Eq. (33) makes the surface an invariant set. Furthermore, it also implies that disturbances or dynamic uncertainties can be tolerated while still keeping the surface an invariant set. The best

https://doi.org/10.1017/S0263574716000709 Published online by Cambridge University Press

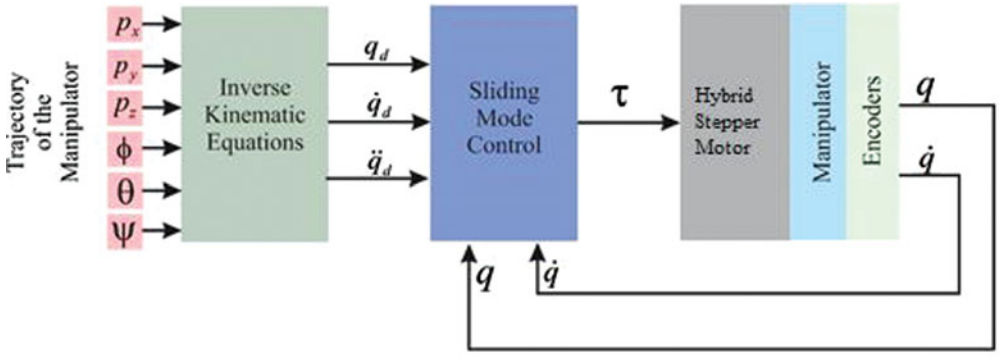

Fig. 7. Block diagram of the sliding mode control implementation.

approximation $\hat{\boldsymbol{\tau}}$ of an equivalent control law that would achieve $\dot{s} = 0$ is thus

$$\hat{\boldsymbol{\tau}} = \hat{\boldsymbol{M}}\ddot{\boldsymbol{q}} + \hat{\boldsymbol{N}} - \boldsymbol{A}\boldsymbol{s} \tag{34}$$

where $\hat{\boldsymbol{M}}$ and $\hat{\boldsymbol{N}}$ are the estimations of $\boldsymbol{M}$ and $\boldsymbol{N}$, $\boldsymbol{A} = diag[a_1, \ldots a_6]$ is also a diagonal positive definite constant matrix. In order to satisfy sliding condition defined in Eq. (33) despite uncertainty on the dynamics, the term $\hat{\boldsymbol{\tau}}$ could be added to discontinuous across the surface. Hence, the control input becomes

$$\boldsymbol{\tau} = \hat{\boldsymbol{\tau}} - \boldsymbol{F}\mathbf{sgn}(\boldsymbol{s}). \tag{35}$$

Substituting Eq. (35) into Eq. (26) leads to

$$\boldsymbol{M}\dot{\boldsymbol{s}} + (\boldsymbol{N} + \boldsymbol{A})\boldsymbol{s} = \boldsymbol{\Delta f} - \boldsymbol{F}\mathbf{sgn}(\boldsymbol{s}) \tag{36}$$

where $\boldsymbol{\Delta f}$ is the estimation error with the definition $\boldsymbol{\Delta f} = (\hat{\boldsymbol{M}} - \boldsymbol{N})\ddot{\boldsymbol{q}} + (\hat{\boldsymbol{N}} - \boldsymbol{N})$ and the estimation error is assumed to be bounded by some known $\boldsymbol{F}$:

$$|\Delta f|_{bound} \leq F. \tag{37}$$

To prove convergence to the sliding mode, $\boldsymbol{s}$ must converge to zero in finite time. For this purpose, the Lyapunov method could be used to obtain a control law that provides stability of the system.

Choosing a Lyapunov function

$$\boldsymbol{V} = \frac{1}{2}\boldsymbol{s}^{\boldsymbol{T}}\boldsymbol{M}\boldsymbol{s}. \tag{38}$$

Since $\boldsymbol{M}$ is the symmetric and positive definite, for $\neq 0$ $\boldsymbol{V} > 0$. And differentiating Eq. (38) and using Eq. (36), it can be proved that

$$\dot{\boldsymbol{V}} = \boldsymbol{s}^{\boldsymbol{T}}\left[-(\boldsymbol{N} + \boldsymbol{A})\boldsymbol{s} + \boldsymbol{\Delta f} - \boldsymbol{F}\mathbf{sgn}(\boldsymbol{s}) + \boldsymbol{N}\boldsymbol{s}\right] = \sum_{i=1}^{n} s_i\left[\boldsymbol{\Delta f}_i - \boldsymbol{F}_i sgn(s_i)\right] - \boldsymbol{s}^{\boldsymbol{T}}\boldsymbol{A}\boldsymbol{s} \leq 0. \tag{39}$$

Using Eq. (37) for $s_i > 0$ and $s_i < 0$ conditions, Eq. (39) provides an exponentially stable system.

In practice, the control law given in Eq. (35) may be resulted in oscillations in high-frequency switching, called chattering. To reduce the control-chattering activity, the high-frequency switching function sgn can be approximated to a smooth bounded saturation function sat.

Figure 7 shows the SMC implementation block diagram of the manipulator that demonstrates the input is the required trajectory of the manipulator in terms of the translation and orientation motions. The controller uses the inverse kinematic equations (5) and (6) to convert the desired position and orientation of the manipulator into the required actuator angles, which are then fed in as the set-points for the six local controllers. The controller then applies the necessary control action to the hybrid

https://doi.org/10.1017/S0263574716000709 Published online by Cambridge University Press

stepper motor drivers, which in turn allows the correct rotations to each input link, achieving the correct angles.

5. Experimental Results

The block diagram of the 6-DOF parallel manipulator control system is shown in Fig. 8. The controller has been implemented using SIMULINK 2014 from MathWorks running on a personal computer with Intel Core i7-4790 3.6 GHz processor. The experiments have been realized using the QPIDe data acquisition device from Quanser that is ideal for rapid control prototyping and delivers superior real-time performance. The QPIDe has 8 analogue inputs/outputs, 56 digital inputs/outputs, 8 user programmable PWM outputs and 8 encoder inputs. The instantaneous HSM motor angles have been measured through the QPIDe encoder inputs using 4x quadrature and the angular velocities have been calculated by the direct backward differentiation method, from the motor angles measured. The resolution of each encoder is 4096 counts per revolution, which yields a resolution of 0.022° for the angular position measurement using 4x quadrature. The modes of the hybrid stepper motor drivers have been set to 1/25600. The control commands, which are the desired torques, have been calculated by SIMULINK program according to the control law, and then these commands have been converted into PWM signals for the hybrid stepper motor drives, the task of which is to drive the PWM phase current signals to generate desired torques.

It is clear that, in the high-frequency reference signal, higher motor output torque is required due to the system dynamics. The maximum output torque capacity of the motors in the designed manipulator system is limited and cannot compensate the output high torques of system dynamics when high speed or high acceleration is needed. Because of this reason, the frequencies of the given reference trajectories in the experiments have been adjusted to low frequencies by taking into consideration of the system load (i.e., load and no load).

For the experimental studies, the LQR controller parameters are $\boldsymbol{K} = [80\ 27.5 \times 10^{-3}]$ and the proposed nonlinear controller parameters have been designed as $\boldsymbol{\lambda} = 18 \quad \eta = 0.1$ and $F = 1.6$. To verify effectiveness of the SMC algorithm with respect to the LQR control, the following experiments have been carried out in two cases.

In the first case, manipulator has been operated with no load, i.e., an external load has not been placed on the moving platform. For the given reference translational trajectories ($x_d = 0.03\sin(\frac{\pi}{10}t)$ [m], $y_d = 0.03\sin(\frac{\pi}{10}t)$ [m]), the results of the position tracking error for the input links with no load have been shown in Fig. 9.

The positioning error of the moving platform can be estimated by obtaining some insight from the input link error shown in Fig. 9. In this case, the position error of the moving platform is not directly measured, but the position error due to the joint error of the input links can be estimated using the Jacobian matrix:[43]

$$x_{error} = J^{-1} q_{error}. \tag{40}$$

Using Eq. (40), estimated position error of the moving platform with respect to the proposed controllers has been shown in Fig. 10.

For the given reference orientation trajectories ($\phi_d = 5\sin(\frac{\pi}{10}t)$ $[deg]$ around x coordinate and $\theta_d = 5\sin(\frac{\pi}{10}t)$ $[deg]$ around y coordinate), the results of the position tracking error for the input links with no load have been shown in Fig. 11.

Using Eq. (40), the estimated orientation error of the moving platform with respect to the proposed controllers has been shown in Fig. 12.

As shown in Figs. 9 and 11, performance of angular displacement error of the input links for the given translational and orientation reference trajectories with no load are improved by using SMC than the LQR method. The same situation occurs for the estimated position and orientation error of the moving platform as shown in Figs. 10 and 12. Additionally, in order to show the efficiency of the SMC, maximum, minimum estimated error and mean square value (MSE) have been calculated with respect to the estimated position and orientation values and outcomes are tabulated in Table II for both trajectories. As illustrated in Table II, the estimated error for maximum and minimum values of x and y position is seen to be less in the SMC method. Same situations can be seen in estimated orientation error and also MSE outcomes.

https://doi.org/10.1017/S0263574716000709 Published online by Cambridge University Press

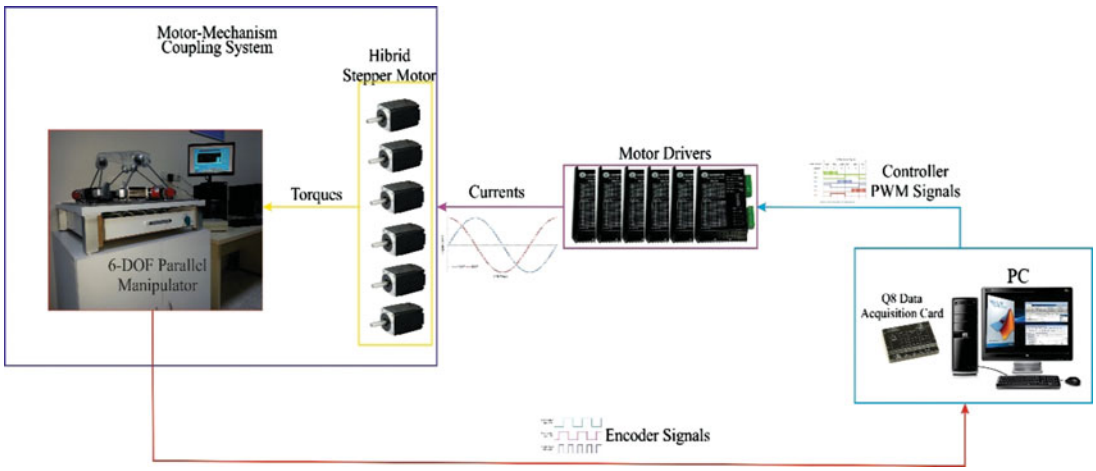

Fig. 8. Block diagram of the 6-DOF parallel manipulator control system.

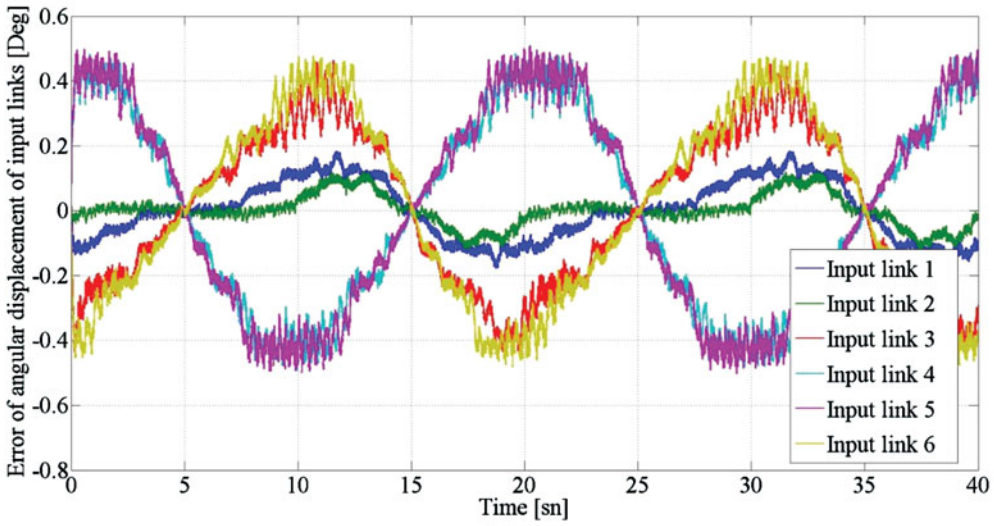

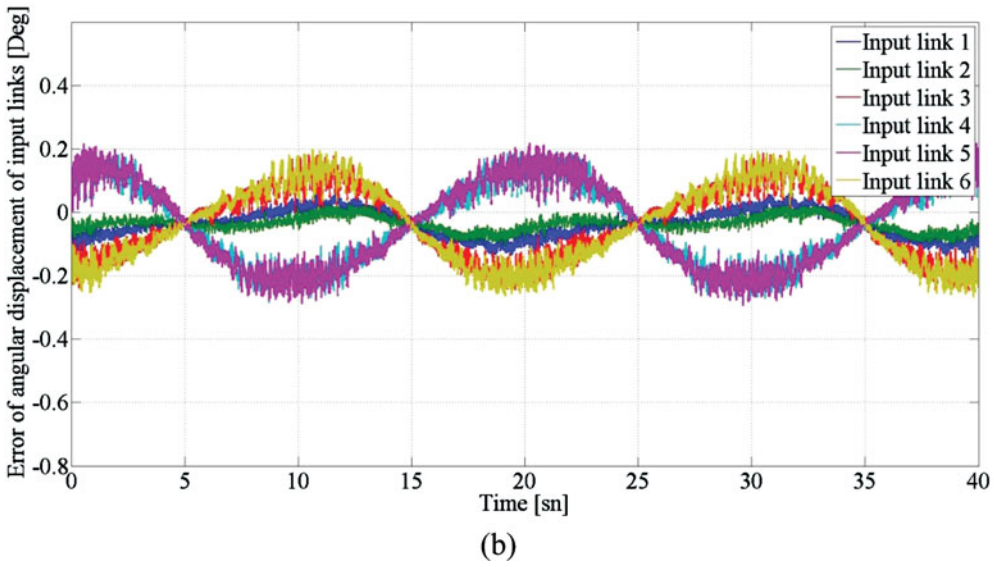

Fig. 9. The error of angular displacement of the input links with no load for the reference translational trajectories ($x_d = 0.03\sin(\frac{\pi}{10}t)$ [m], $y_d = 0.03\sin(\frac{\pi}{10}t)$ [m]). (a) With LQR controller. (b) With sliding mode controller.

https://doi.org/10.1017/S0263574716000709 Published online by Cambridge University Press

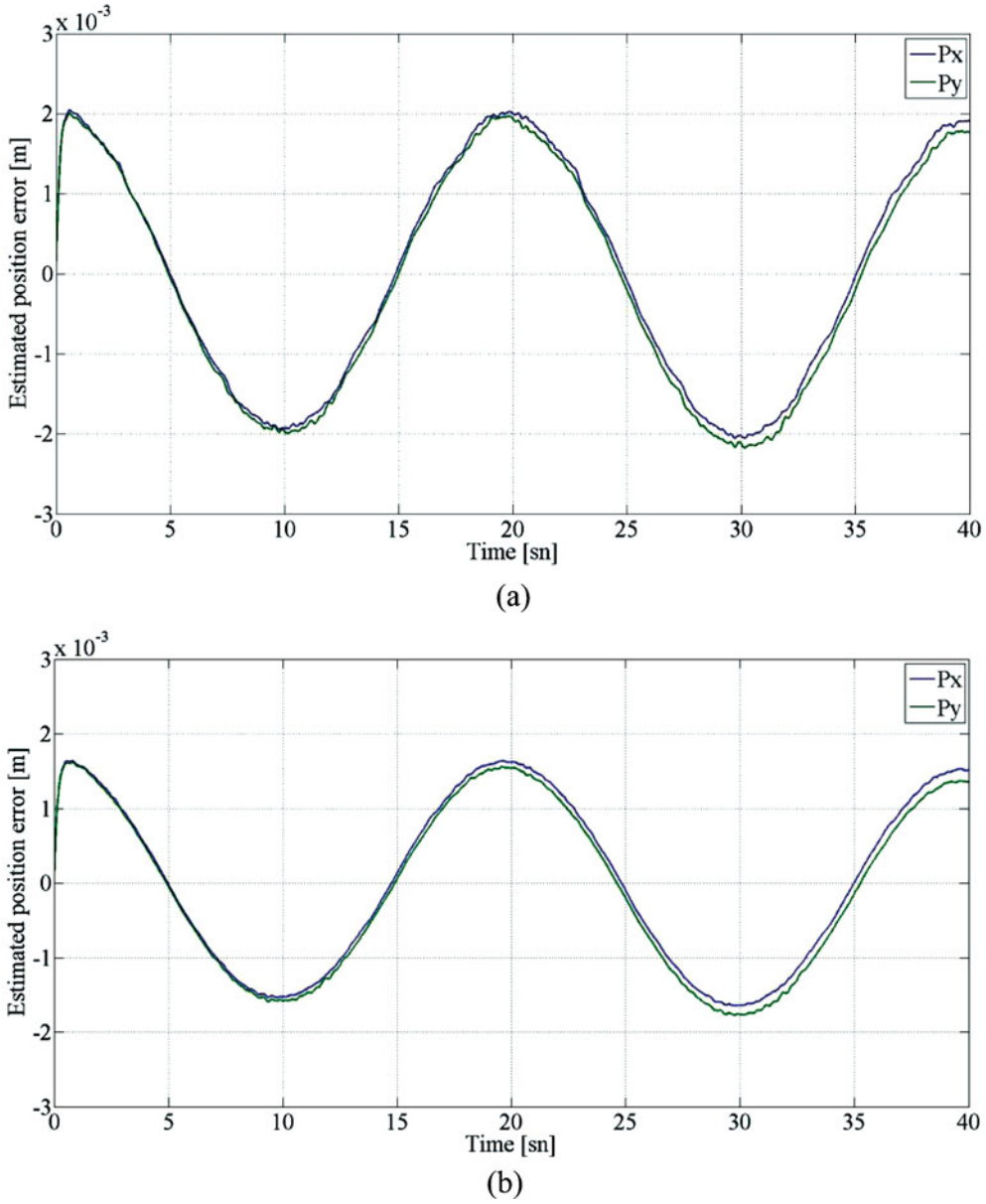

Fig. 10. The estimated position error of the moving platform with no load for the reference translational trajectories ($x_d = 0.03\sin(\frac{\pi}{10}t)$ [m], $y_d = 0.03\sin(\frac{\pi}{10}t)$ [m]). (a) With LQR controller. (b) With sliding mode controller.

In the second case, manipulator has been operated with a load, i.e., an external load of $0.2\,kg$ has been placed on the moving platform. In this case, to compensate the motor output torques, the frequencies of the given reference trajectories for experiments have been adjusted slightly lower than the case I with no load. In the performed experimental studies with considered load, the reference signal frequency has been determined as maximum $1/30$ Hz.

For the given reference translational trajectories ($x_d = 0.03\sin(\frac{\pi}{15}t)\,[m]$, $y_d = 0.03\ \sin(\frac{\pi}{15}t)\,[m]$), the results of the position tracking error for the input links with a load have been shown in Fig. 13.

Using Eq. (40), the estimated position error of the moving platform with respect to the proposed controllers has been shown in Fig. 14.

For the given reference orientation trajectories ($\phi_d = 5\sin(\frac{\pi}{15}t)\ [deg]$ around x coordinate and $\theta_d = 5\sin(\frac{\pi}{15}t)\ [deg]$ around y coordinate), the results of the position tracking error for the input links with a load have been shown in Fig. 15.

https://doi.org/10.1017/S0263574716000709 Published online by Cambridge University Press

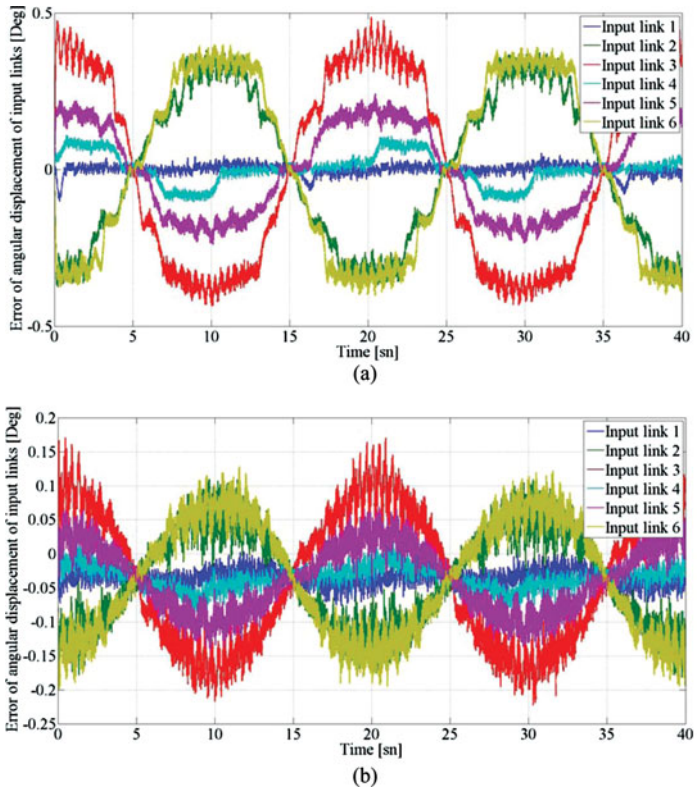

Fig. 11. The error of angular displacement of the input links with no load for the reference orientation trajectories ($\phi_d = 5\sin(\frac{\pi}{10}t)\ [deg]$, $\theta_d = 5\sin(\frac{\pi}{10}t)\ [deg]$). (a) With LQR controller. (b) With sliding mode controller.

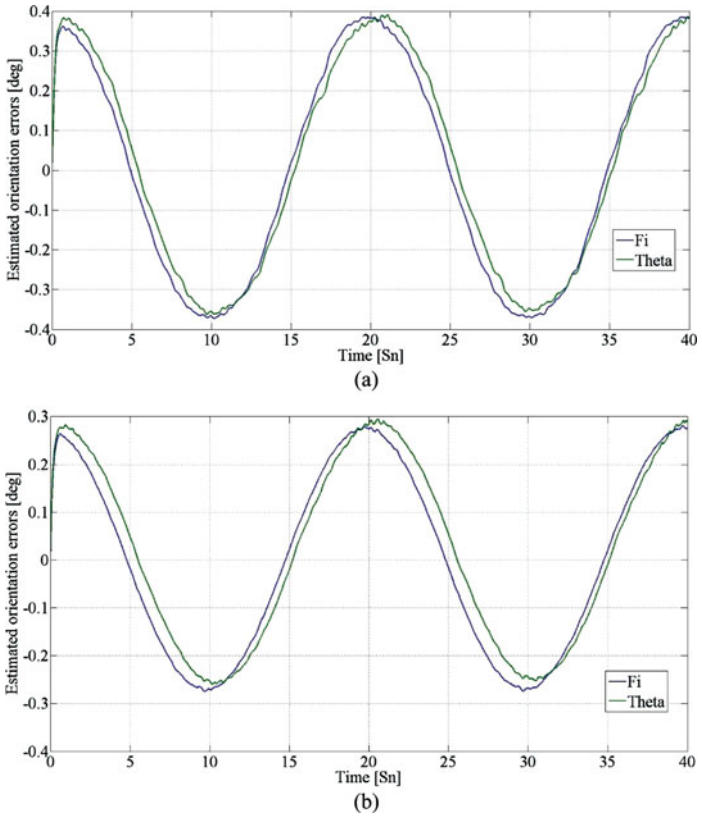

Fig. 12. The estimated orientation error of the moving platform with no load for the reference orientation trajectories ($\phi_d = 5\sin(\frac{\pi}{10}t)\ [deg]$, $\theta_d = 5\sin(\frac{\pi}{10}t)\ [deg]$). (a) With LQR controller. (b) With sliding mode controller.

https://doi.org/10.1017/S0263574716000709 Published online by Cambridge University Press

Table II. Performance summary for case I.

Translational reference trajectories $x_d = 0.03\sin(\frac{\pi}{10}t)$ $[m]$, $y_d = 0.03\sin(\frac{\pi}{10}t)$ $[m]$ with no load	Sliding mode control	LQR control
Max. X Position Error (m)	0.0016	0.002
Max. Y Position Error (m)	0.0016	0.002
Min. X Position Error (m*r*)	−0.0016	−0.0021
Min. Y Position Error (m)	−0.0018	−0.0022
X Position MSE Value	1.29670E–06	1.96060E–06
Y Position MSE Value	1.30870E–06	1.99350E–06
Orientation reference trajectories of $\phi_d = 5\sin(\frac{\pi}{10}t)$ $[deg]$ around $\boldsymbol{x}$ coordinate and $\theta_d = 5\sin(\frac{\pi}{10}t)$ $[deg]$ around $\boldsymbol{y}$ coordinate with no load		
	Sliding mode control	LQR control
Max. ϕ orientation error (deg)	0.2814	0.3856
Max. θ orientation error (deg)	0.2939	0.3914
Min. ϕ orientation error (deg)	−0.2747	−0.373
Min. θ orientation error (deg)	−0.2601	−0.3628
ϕ orientation MSE value	6.5327E–04	0.0013
θ orientation MSE value	6.4479E–04	0.0012

Table III. Performance summary for case II.

Translational reference trajectories $x_d = 0.03\sin(\frac{\pi}{15}t)$ $[m]$, $y_d = 0.03\sin(\frac{\pi}{15}t)$ $[m]$ with a load	Sliding mode control	LQR control
Max. X position error (m)	6.7364E–04	0.0017
Max. Y position error (m)	6.6493E–04	0.0017
Min. X position error (m)	−6.3295E-04	−0.0016
Min. Y position error (m)	−6.5496E-04	−0.0016
X position MSE value	2.2321E–07	1.2924E–06
Y position MSE value	2.1853E–07	1.2789E–06
Orientation reference trajectories of $\boldsymbol{\phi_d} = 5\sin(\frac{\pi}{15}t)$ $[deg]$ around $\boldsymbol{x}$ coordinate and $\boldsymbol{\theta_d} = 5sin(\frac{\pi}{15}\boldsymbol{t})$ $[deg]$ around $\boldsymbol{y}$ coordinate with a load		
	Sliding mode control	LQR control
Max. ϕ orientation error (deg)	0.0513	0.1889
Max. θ orientation error (deg)	0.0570	0.2035
Min. ϕ orientation error (deg)	−0.0482	−0.1822
Min. θ orientation error (deg)	−0.0503	−0.1815
ϕ orientation MSE value	2.0966E–05	2.9709E–04
θ orientation MSE value	2.6284E–05	3.3151E–04

Using Eq. (40), the estimated orientation error of the moving platform with respect to the proposed controllers has been shown in Fig. 16.

As shown in Figs 13–16 and Table III, performance of angular displacement error of the input links for the given reference trajectories with an external load is improved by using the SMC than using LQR method. In addition to these outcomes, the results of the case II are better than the results of the case I because of decreasing the frequency of the reference signal trajectories. In the second

https://doi.org/10.1017/S0263574716000709 Published online by Cambridge University Press

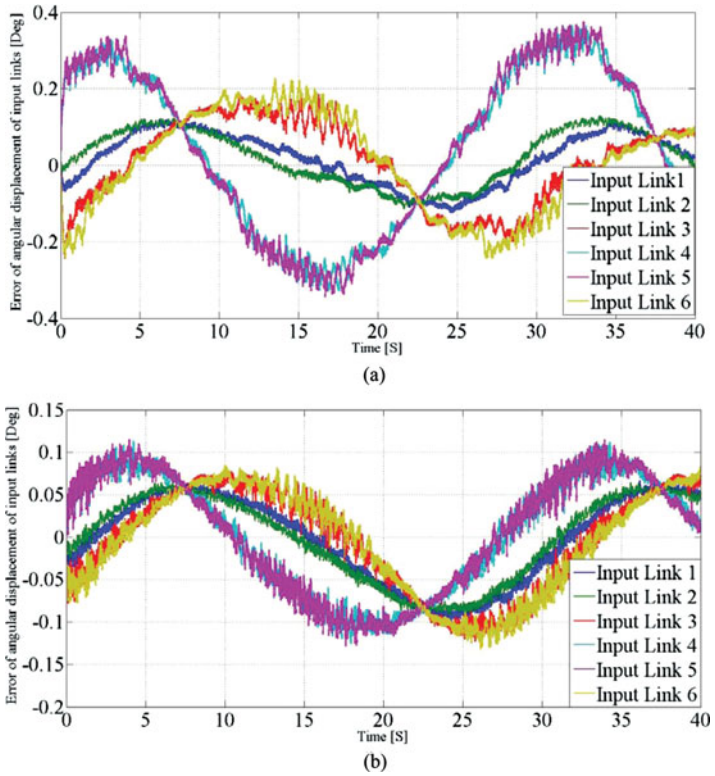

Fig. 13. The error of angular displacement of the input links with a load for the reference translational trajectories ($x_d = 0.03\sin(\frac{\pi}{15}t)$ $[m]$, $y_d = 0.03\sin(\frac{\pi}{15}t)$ $[m]$). (a) With LQR controller. (b) With sliding mode controller.

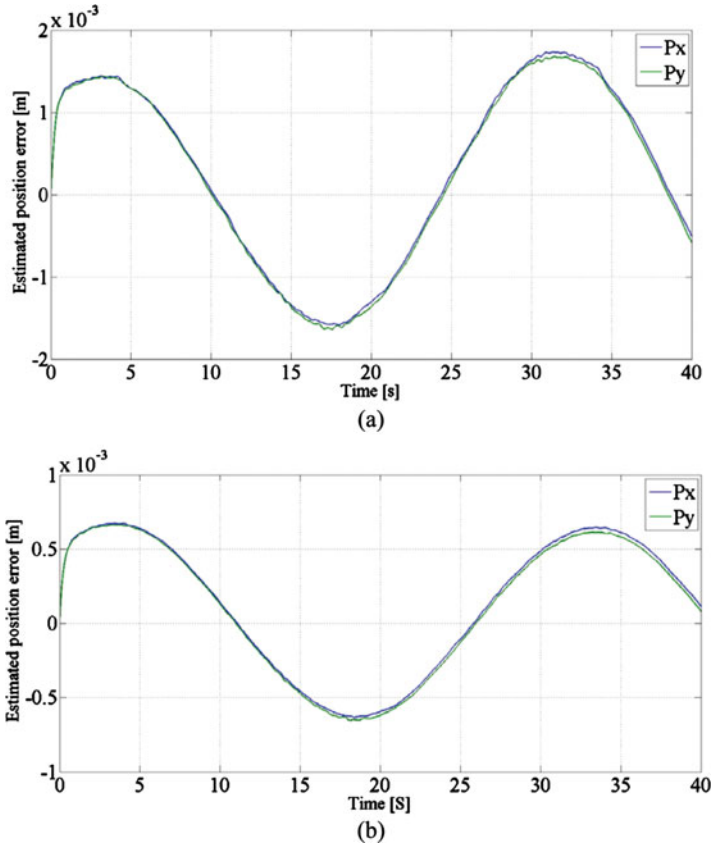

Fig. 14. The estimated position error of the moving platform with a load for the reference translational trajectories ($x_d = 0.03\sin(\frac{\pi}{15}t)$ $[m]$, $y_d = 0.03\sin(\frac{\pi}{15}t)$ $[m]$). (a) With LQR controller. (b) With sliding mode controller.

https://doi.org/10.1017/S0263574716000709 Published online by Cambridge University Press

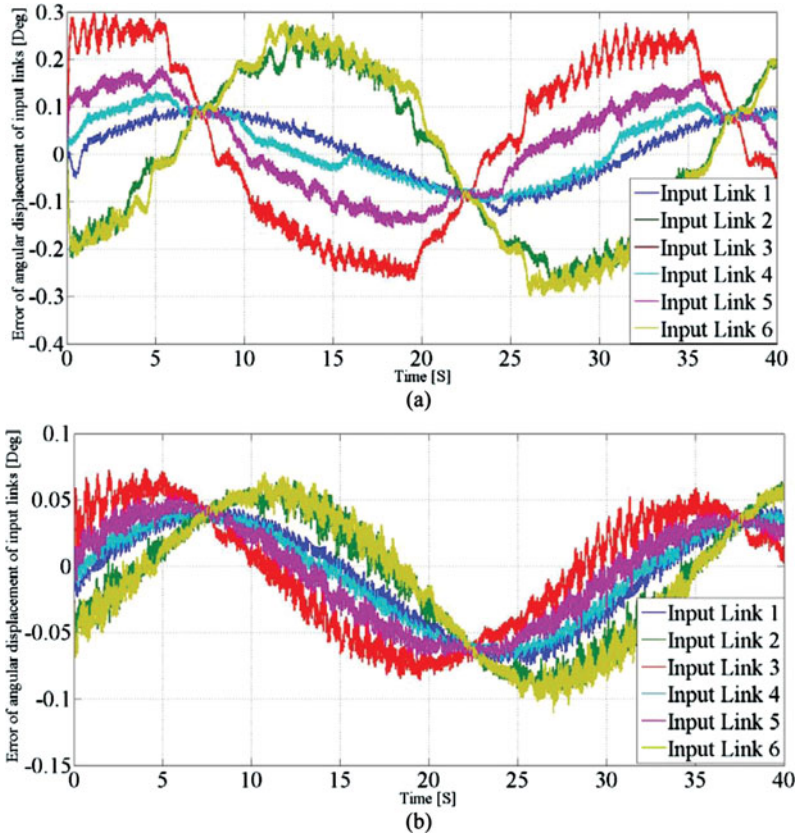

Fig. 15. The error of angular displacement of the input links with a load for the reference orientation trajectories ($\phi_d = 5\sin(\frac{\pi}{15}t)\ [deg]$, $\theta_d = 5\sin(\frac{\pi}{15}t)\ [deg]$). (a) With LQR controller. (b) With sliding mode controller.

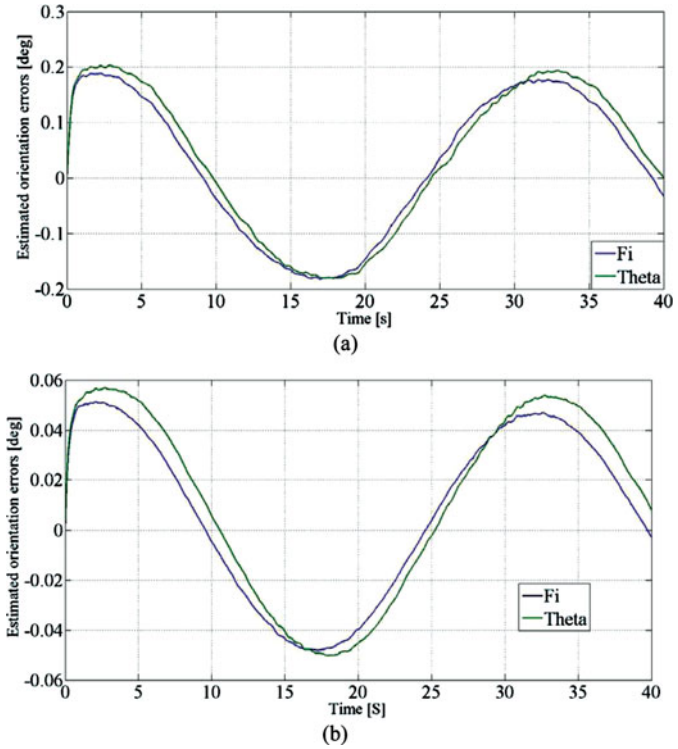

Fig. 16. The estimated orientation error of the moving platform with a load for the reference orientation trajectories ($\phi_d = 5\sin(\frac{\pi}{15}t)\ [deg]$, $\theta_d = 5\sin(\frac{\pi}{15}t)\ [deg]$). (a) With LQR controller. (b) With sliding mode controller.

https://doi.org/10.1017/S0263574716000709 Published online by Cambridge University Press

case, the SMC has been performed more effectively than the LQR control, because of its efficient, robust control characteristic for unknown loads and un-modelled dynamics.

6. Conclusions

In this paper, a 6-DOF 6-RSS parallel manipulator has been designed. Tracking control of the manipulator based on a linear quadratic optimal regulator and the nonlinear sliding mode controller for given different trajectories has been developed and validated through experimental results. First, the architecture of the designed manipulator has been introduced and then mathematical modelling of the manipulator has been analysed. In order to investigate the effects of the manipulator dynamics and control techniques, two modelling approaches have been developed. The first approach is based on the SISO modelling and the second approach is the decoupled dynamic model approximation. Both dynamic modelling techniques have been combined with hybrid stepper motor dynamics. Then, in order to investigate the effects of different control approaches on the improvement of the tracking performance of the manipulator, linear quadratic optimal regulator and nonlinear SMC approaches have been utilized. Finally, it has been validated experimentally that SMC is an efficient, robust control method for the manipulator including un-modelled dynamics.

References

1. J. P. Merlet, *Parallel Robots* (Springer, New York, 2006).
2. J. S. Dai, Z. Huang and H. Lipkin, "Mobility of over constrained parallel mechanisms," *J. Mech. Des.* **128**(1), 220–229 (2006).
3. D. Stewart, "A platform with six degrees of freedom," *Proc. Inst. Mech. Eng.* **180**(1), 371–386 (1965).
4. L. Yangmin and X. Qingsong, "Design and development of a medical parallel robot for cardiopulmonary resuscitation," *IEEE/ASME Trans. Mechatronics* **12**(3), 265–273 (2007).
5. M. Shoham, M. Burman, E. Zehavi, L. Joskowicz, E. Batkilin and Y. Kunicher, "Bone-mounted miniature robot for surgical procedures: Concept and clinical applications," *IEEE Trans. Robot. Autom.* **19**(5), 893–901 (2003).
6. W. L. Xu, J. S. Pap and J. Bronlund, "Design of a biologically inspired parallel robot for foods chewing," *IEEE Trans. Ind. Electron.* **55**(2), 832–841 (2008).
7. K. Ibrahim, A. Ramadan, M. Fanni, Y. Kobayashi, A. Abo-Ismail and M. G. Fujie, "Development of a new 4-DOF endoscopic parallel manipulator based on screw theory for laparoscopic surgery," *Mechatronics* **28**, 4–7 (2015).
8. E. Ottaviano and M. Ceccarelli, "Application of a 3-DOF parallel manipulator for earthquake simulations," *IEEE/ASME Trans. Mechatronics* **11**(2), 241–246 (2006).
9. L. Kok-Meng and S. Arjunan, "A three-degrees-of-freedom micromotion in-parallel actuated manipulator," *IEEE Trans. Robot. Autom.* **7**(5), 634–641 (1991).
10. A. A. Ramadan, T. Takubo, Y. Mae, K. Oohara and T. Arai, "Developmental process of a chopstick-like hybrid-structure two-fingered micromanipulator hand for 3-D manipulation of microscopic objects," *IEEE Trans. Ind. Electron.* **56**(4), 1121–1135 (2009).
11. F. J. Berenguer and F. M. Monasterio-Huelin, "Zappa, a quasi-passive biped walking robot with a tail: modeling, behavior, and kinematic estimation using accelerometers," *IEEE Trans. Ind. Electron.* **55**(9), 3281–3289 (2008).
12. F. Pierrot, V. Nabat, O. Company, S. Krut and P. Poignet, "Optimal design of a 4-DOF parallel manipulator: from academia to industry," *IEEE Trans. Robot.* **25**(2), 213–224 (2009).
13. T. Huang, D. G. Chetwynd, J. P. Mei and X. M. Zhao, "Tolerance design of a 2-DOF over constrained translational parallel robot," *IEEE Trans. Robot.* **22**(1), 167–172 (2006).
14. S.-H. Chen and L.-C. Fu, "Observer-based backstepping control of a 6-dof parallel hydraulic manipulator," *Control Eng. Pract.* **36**(0), 100–112 (2015).
15. Y. Pi and X. Wang, "Trajectory tracking control of a 6-DOF hydraulic parallel robot manipulator with uncertain load disturbances," *Control Eng. Pract.* **19**(2), 185–193 (2011).
16. E. Castillo-Castañeda and Y. Takeda, "Improving path accuracy of a crank-type 6-dof parallel mechanism by stiction compensation," *Mech. Mach. Theory* **43**(1), 104–114 (2008).
17. W. L. Xu, J. D. Torrance, B. Q. Chen, J. Potgieter, J. E. Bronlund and J. S. Pap, "Kinematics and experiments of a life-sized masticatory robot for characterizing food texture," *IEEE Trans. Ind. Electron.* **55**(5), 2121–2132 (2008).
18. A. Dumlu and K. Erenturk, "Modeling and trajectory tracking control of 6-DOF RSS type parallel manipulator," *Robotica* **32**(04), 643–657 (2014).
19. X. J. Liu, J. Wang, F. Gau and L. P. Wang, "Mechanism design of a simplified 6-DOF 6-RUS parallel manipulator," *Robotica* **20**(01), 81–91 (2002).
20. Z. Yang, J. Wu and J. Mei, "Motor-mechanism dynamic model based neural network optimized computed torque control of a high speed parallel manipulator," *Mechatronics* **17**(7), 381–390 (2007).

https://doi.org/10.1017/S0263574716000709 Published online by Cambridge University Press

21. A. Codourey and T. Yoshikawa, "Dynamic Modelling and Mass Matrix Evaluation of the DELTA Parallel Robot for Axes Decoupling Control," *Proceedings of the IEEE/RSJ International Conference on Intelligent Robots and Systems*, (1996) pp. 1211-1218.
22. A. Albagul and D. Wahyu, "Dynamic Modeling and Adaptive Traction Control for Mobile Robots," *Proceedings of the Ind. Elec. Soc. 30th Annual of the IEEE/IECON*, (2004) pp. 614–620.
23. Y. Ting, C. C. Li and T. V. Nquyen, "Composite controller design for a 6DOF Stewart nanoscale platform," *Precis. Eng.* **37**(03), 671–683 (2013).
24. Y. Su, D. Sun, L. Ren, and J. K. Mills, "Integration of saturated PI synchronous control and PD feedback for control of parallel manipulators," *IEEE Trans. Robot.* **22**(1), 202–207 (2006).
25. K. S. Grewal, D. Dixon and J. Pearson, "LQG controller design applied to a pneumatic stewart-gough platform," *Int. J. Autom. Comput.* **9**(1), 45–53 (2012).
26. I. Davliakos and E. Papadopoulos, "Model-based control of a 6-dof electrohydraulic Stewart-gough platform," *Mech. Mach. Theory* **43**(11), 1385–1400 (2008).
27. I. Davliakos and E. Papadopoulos, "Impedance model-based control for an electrohydraulic Stewart platform," *Eur. J. Control* **5**(5), 560–577 (2009).
28. Q. Meng, T. Zhang, J. He, J. Song and X. Chen, "Improved model-based control of a six-degree-of-freedom Stewart platform driven by permanent magnet synchronous motors," *Ind. Robot: An Int. J.* **39**(1), 47–56 (2012).
29. C. F. Yang, Q. T. Huang, and J. W. Han, "Decoupling control for spatial six-degree-of-freedom electro-hydraulic parallel robot," *Robot. Comput.-Integr. Manuf.* **28**(1), 14–23 (2012).
30. S. H. Lee, J. B. Song, W. C. Choi and S. Hong, "Position control of a Stewart platform using inverse dynamics control with approximate dynamics," *Mechatronics* **13**(6), 605–619 (2003).
31. Y. Xu, H. Liao, L. Liu and Y. Wang, "Modeling and robust H-infinite control of a novel non-contact ultra-quiet Stewart spacecraft," *Acta Astronautica* **107**(01), 274–289 (2015).
32. A. Zubizarreta, M. Marcos, I. Cabanes and C. Pinto, "A procedure to evaluate extended computed torque control configurations in the Stewart–Gough platform," *Robot. Auton. Syst.* **59**(10), 770–781 (2011).
33. S. Kizir and Z. Bingül, "Fuzzy impedance and force control of a Stewart platform," *Turkish J. Electr. Eng. Comput. Sci.* **22**(01), 924–939 (2014).
34. H. Guo, Y. Liu, G. Liu and H. Li, "Cascade control of a hydraulically driven 6-DOF parallel robot manipulator based on a sliding mode," *Control Eng. Pract.* **16**(9), 1055–1068 (2008).
35. C. Sung-Hua and F. Li-Chen, "Output feedback sliding mode control for a stewart platform with a nonlinear observer-based forward kinematics solution," *IEEE Trans. Control Systems Technology* **21**(1), 176–185 (2013).
36. M. Qiang, Z. Tao, G. Xiang and S. Jing-yan, "Adaptive sliding mode fault-tolerant control of the uncertain stewart platform based on offline multibody dynamics," *IEEE/ASME Trans. Mechatronics* **19**(3), 882–894 (2014).
37. N.-I. Kim, C.-W. Lee and P.-H. Chang, "Sliding mode control with perturbation estimation: Application to motion control of parallel manipulator," *Control Eng. Pract.* **6**(11), 1321–1330 (1998).
38. C. Edwards and S. Spurgeon, *Sliding Mode Control: Theory and Applications* (London: Taylor and Francis, 1998).
39. V. Utkin, "Variable structure systems with sliding modes," *IEEE Trans. Autom. Control* **22**(2), 212–222 (1977).
40. J. J. E. Slotine and W. Li, *Applied Nonlinear Control* (New Jersey: Prentice-Hall, 1991).
41. A. Bellini, C. Concari, G. Franceschini and A. Toscani, "Mixed-mode PWM for high-performance stepping motors," *IEEE Trans. Ind. Electron.* **54**(6), 3167–3177 (2007).
42. S. Islam and P. X. Liu, "Robust sliding mode control for robot manipulators," *IEEE Trans. Ind. Electron.* **58**(6), 2444–2453 (2011).
43. M. M. Fateh and H. Farhangfard, "On the transforming of control space by manipulator Jacobian," *Int. J. Control Autom.* **6**(1), 101–108 (2008).

https://doi.org/10.1017/S0263574716000709 Published online by Cambridge University Press